別紙４

研究成果の刊行に関する一覧表

雑誌

発表者氏名	論文タイトル名	発表誌名	巻号	ページ	出版年
Hiraiwa, K., Ueda, M., Takeuchi, H., Oyama, T., Irino, T., Yoshikawa, T., Kondo, A., Kitagawa, Y.	Sentinel node mapping with thermoresponsive magnetic nanoparticles in rats	*Journal of Surgical Research*	174	48-55	2012
Nishimura, Y., Shishido, T., Ishii, J., Tanaka, T., Ogino, C., Kondo, A.	Protein-encapsulated bio-nanocapsules production with ER membrane localization sequences	*Journal of Biotechnology*	157(1)	124-129	2012
Ninomiya, K., Ogino, C., Oshima, S., Sonoke, S., Kuroda, S., Shimizu, N.	Targeted sonodynamic therapy using protein-modified TiO2 nanoparticles	*Ultrasonics Sonochemistry*	19(3)	607-614	2012
Nishimura, Y., Ishii, J., Okazaki, F., Ogino, C., Kondo, A.	Complex carriers of affibody-displaying bio-nanocapsules and composition -varied liposomes for HER2-expressing breast cancer celll-specific protein delivery	*Journal of Drug Targeting*	20(10)	897-905	2012
Nishimura, Y., Mimura, W., Fahimuddin, I.., Amino, T., Ishii, J., Ogino C., Kondo, A.	Granting specificity for breast cancer cells using a Hepatitis B core particle with a HER2-targeted affibody molecule	*Journal of Biochemistry*	153(3)	251-256	2013
Nishimura, Y., Takeda, K., Ishii, J., Ogino, C., Kondo, A.	An affinity chromatography method used to purify His-tag-displaying bio-nanocapsules	*Journal of Virological Methods*	189(2)	393-396	2013
Ninomiya, K., Aikawa, M., Ogino, C., Shimizu, N.	Inactivation of Escherichia coli by sonoelectrocatalytic disinfection using TiO2 as electrode	*Ultrasonics Sonochemistry*	20(2)	762-767	2013

Ninomiya, K., Kaneda, K., Kawashima, S., Miyachi, Y., Ogino, C., Shimizu, N.	Cell-SELEX based selection and characterization of DNA apatamer recognizing human hepatocarcinoma	*Bioorganic & Medicinal Chemistry*	23(6)	1797-1802	2013
Srivastava, S.K., Yamada, R., Ogino, C., Kondo, A.	Sidewall modification of multiwalled carbon nanotubes by Allivum sativum (garlic) and its effect on the deposition of gold nanoparticles	*Carbon*	56	309-316	2013
Srivastava, S.K., Yamada, R., Ogino, C., Kondo, A.	Biogenic synthesis and characterization of gold nanoparticles by Escherichia coli K12 and its heterogeneous catalysis in degradation of 4-nitrophenol	*Nanoscale Research Letter*	8(1)	70	2013
J. Han, S. Ohara, K. Sato, H. Xu, Z. Tan, Y. Morisada, K. Kuruma, M. Naito, P. Shan, and M. Umetsu	Directed Assembly of Metal Oxide Nanoparticles by DNA	*Mater. Lett.*	79	78-80	2012
Iwata H, Demizu Y, Fujii O, Terashima K, Mima M, Niwa Y, Hashimoto N, Akagi T, Sasaki R, Hishikawa Y, Abe M, Shibamoto Y, Murakami M, Fuwa N.	Long-Term Outcome of Proton Therapy and Carbon-Ion Therapy for Large (T2a-T2bN0M0) Non-Small-Cell Lung Cancer	*J Thorac Oncol.*	8(6)	726-735	2013
Akasaka H, Sasaki R, Yoshida K, Takayama I, Yamaguchi T, Yoshida H, Mizushina Y.	Monogalactosyl diacylglycerol, a replicative DNA polymerase inhibitor, from spinach enhances the anti-cell proliferation effect of gemcitabine in human pancreatic cancer cells	*Biochim Biophys Acta.*	1830	2517-2525	2013
Nishimura H, Sasaki R, Yoshida K, Miyawaki D, Okamoto Y, Kiyota N, Saito M, Otsuki N, Nibu KI.	Radiotherapy for Stage I or II hypopharyngeal carcinoma	*J Radiat Res.*	53(6)	892-9	2012
Tamaki Y, Sasaki R, Ejima Y, Ogura M, Negoro Y, Nakajima T, Murakami M, Kaji Y, Sugimura K.	Efficacy of intraoperative radiotherapy targeted to the abdominal lymph node area in patients with esophageal carcinoma	*J Radiat Res.*	53(6)	882-91	2012

Uehara K, Sasayama T, Miyawaki D, Nishimura H, Yoshida K, Okamoto Y, Mukumoto N, Akasaka H, Nishihara M, Fujii O, Soejima T, Sugimura K, Kohmura E, Sasaki R.	Patterns of failure after multimodal treatments for high-grade glioma: effectiveness of MIB-1 labeling index	*Radiat Oncol.*	7	104	2012
Ishihara T, Yoden E, Konishi K, Nagase N, Yoshida K, Kurebayashi J, Sonoo H, Murashima N, Sasaki R, Hiratsuka J.	Long-term outcome of hypofractionated radiotherapy to the whole breast of Japanese women after breast-conserving surgery	*Breast Cancer.*			
Terashima K, Demizu Y, Hashimoto N, Jin D, Mima M, Fujii O, Niwa Y, Takatori K, Kitajima N, Sirakawa S, Yonson K, Hishikawa Y, Abe M, Sasaki R, Sugimura K, Murakami M.	A phase I/II study of gemcitabine-concurrent proton radiotherapy for locally advanced pancreatic cancer without distant metastasis	*Radiother Oncol.*	103(1)	25-31	2012
Hashimoto N, Sasaki R, Nishimura H, Yoshida K, Miyawaki D, Nakayama M, Uehara K, Okamoto Y, Ejima Y, Azumi A, Matsui T, Sugimura K.	Long-term Outcome and Patterns of Failure in Primary Ocular Adnexal MALT Lymphoma Treated with Radiotherapy.	*Int. J Radiat Oncol Biol Phys*	82(4)	1509-14	2012
Sasaki R, Yasuda K, Abe E, Uchida N, Kawashima M, Uno T, Fujiwara M, Shioyama Y, Kagami Y, Shibamoto Y, Nakata K, Takada Y, Kawabe T, Uehara K, Nibu K, Yamada S.	Multi-institutional Analysis of Solitary Extramedullary Plasmacytoma of the Head and Neck Treated with Curative Radiotherapy	*Int J Radiat Oncol Biol Phys,*	82(2)	626-34	2012

A. Sahraneshin, S. Asahina, T. Togashi, V. Singh, S. Takami, D. Hojo, T. Arita, K. Minami, T. Adschiri	Surfactant-Assisted Hydrothermal Synthesis of Water-Dispersible Hafnium Oxide Nanoparticles in Highly Alkaline Media	*Cryst. Growth Des.*	12	5219-5226	2012
A. Sahraneshin, S. Takami, D. Hojo, T. Arita, K. Minami, T. Adschiri	Mechanistic study on the synthesis of one-dimensional yttrium aluminum garnet nanostructures under supercritical hydrothermal conditions in the presence of organic amines	*CrystEngComm*	14	6085-6092	2012
Daniel Oliveira, Do-Myoung Kim, Mistuo Umetsu, Izumi Kumagai, Tadafumi Adschiri, and Winfried Teizer	The assembly of kinesin-based nanotransport systems	*Journal of Applied Physics*	112	124703(1-8)	2012
Aurélien Sikora, Daniel Oliveira, Kyongwan Kim, Andrew L. Liao, Mitsuo Umetsu, Izumi Kumagai, Tadafumi Adschiri, Wonmuk Hwang, and Winfried Teizer	Quantum Dot Motion on Microtubules	*Chemistry Letters*	41	1215-1217	2012
Takamitsu Hattori, Mitsuo Umetsu, Takeshi Nakanishi, Satoko Sawai, Shinsuke Kikuchi, Ryutaro Asano, and Izumi Kumagai	A high-affinity gold-binding camel antibody: Antibody engineering for one-pot functionalization of gold nanoparticles as biointerface molecules	*Bioconjugate Chemistry*	23	1934-1944	2012
Jinghua Han, Satoshi Ohara, Kaduyoshi Sato, Hui Xu, Zhenquan Tan, Yoshiaki Morisada, Kazuo Kuruma, Makio Naito, Ping Shan, Mitsuo Umetsu	Directed assembly of metal oxide nanoparticles by DNA	*Materials Letters*	79	78-80	2012

Ryutaro Asano, Makoto Nakayama, Hiroko Kawaguchi, Tsuguo Kubota, Takeshi Nakanishi, Mitsuo Umetsu, Hiroki Hayashi, Yu Katayose, Michiaki Unno, Toshio Kudo, and Izumi Kumagai	Construction and humanization of a functional bispecific EGFR CD16 diabody using a refolding system	*FEBS Journal*	279(2)	223-233	2012
Eva Hemmer, Hiroyuki Takeshita, Tomoyoshi Yamano, Takanori Fujiki, Yvonne Kohl, Karin Low, Nallusamy Venkatachalam, Hiroshi Hyodo, Hidehiro Kishimoto and Kohei Soga	in vitro and in vivo investigations of upconversion and NIR emitting Gd2O3:Er3+,Yb3+ nanostructures for biomedical applications	*Journal of Materials Science-Materials in Medicine*	23	2399-2412	2012
Kohei Soga, Kimikazu Tokuzen, Keisuke Fukuda, Hiroshi Hyodo, Eva Hemmer, Nallusamy Venkatachalm, Hidehiro Kishimoto	Application of Ceramic/Polymer Conjugate Materials for Near Infrared Biophotonics	*Journal of Photopolymer Science and Technology*	25	57-62	2012

Journal of Surgical Research **174,** 48–55 (2012)
doi:10.1016/j.jss.2010.11.884

Sentinel Node Mapping with Thermoresponsive Magnetic Nanoparticles in Rats

Kunihiko Hiraiwa, M.D.,* Masakazu Ueda, M.D., Ph.D.,*,[1] Hiroya Takeuchi, M.D., Ph.D.,* Takashi Oyama, M.D.,* Tomoyuki Irino, M.D.,* Takahisa Yoshikawa, M.D.,* Akihiko Kondo, Ph.D.,† and Yuko Kitagawa, M.D., Ph.D.*

**Department of Surgery, Keio University School of Medicine, Shinjuku, Tokyo, Japan; and †Department of Chemical Science and Engineering, Graduate School of Engineering, Kobe University, Nada, Kobe, Japan*

Originally submitted June 4, 2010; accepted for publication November 9, 2010

Background. **In this study, we investigated the ability of magnetic resonance imaging (MRI) after interstitial administration of thermoresponsive magnetic nanoparticles to detect the sentinel lymph node (SLN).**

Materials and Methods. **Postcontrast MRI scans were acquired following subcutaneous injection of thermoresponsive magnetic nanoparticles into the thoracic wall of rats. The signal-to-noise ratio of axillary lymph nodes was calculated to assess whether the SLN could be detected by MRI. In a second experiment, after injecting thermoresponsive magnetic nanoparticles, i.e., Therma-Max 36, Therma-Max 42, Therma-Max 55, and Ferridex, into the subserosa of the cecum of rats, the injection sites, the SLNs, and the distant lymph nodes were resected and examined histologically in order to determine which nanoparticles, if any, were specifically retained in the SLN.**

Results. **MRI showed that the signal-to-noise ratio of axillary SLNs was significantly lower 24 h after injection of Therma-Max 42 than on the precontrast images ($P < 0.05$). Histologic evaluation revealed that Therma-Max 36 aggregated at body temperature and did not migrate to the SLN. Therma-Max 42, on the other hand, aggregated, and the particles became large enough to be retained in the SLNs. Therma-Max 55 and Ferridex did not aggregate, and they both migrated to the SLNs and the distant lymph nodes.**

Conclusions. **The results of this study showed that thermoresponsive magnetic nanoparticles could be targeted to the SLN by adjusting the temperature at which they aggregate, and that they could be used as a contrast agent for SLN mapping by MRI.**

Key Words: **sentinel lymph node; thermoresponsive magnetic nanoparticle; magnet resonance imaging; lymphography.**

INTRODUCTION

Determination whether tumor cells have spread to lymph nodes plays an important role in staging cancer and in designing appropriate treatment protocols. Axillary node metastasis is an important prognostic indicator in breast cancer. The sentinel lymph node (SLN) is defined as the first lymph node to which lymph from the primary tumor drains, and it is therefore at highest risk for regional metastasis *via* lymphatic spread. Surgical biopsy of the SLN is now becoming standard practice for minimally invasive surgery in early stage breast cancer because of the proven accuracy of staging [1–3], and it is useful for planning the operative field and selective lymphadenectomy, and for avoiding unnecessary extended lymphadenectomies. As a result, surgery on the basis of the SLN concept improves the postoperative quality of life of patients.

The lymphoscintigraphic method and blue dye method are currently the most widely used methods of identifying the SLN for biopsy in breast cancer patients [3], but there are some disadvantages and potential pitfalls in SLN mapping by these methods. The scintigraphic method is unavailable in hospitals that do not have a nuclear medicine department, and it has the disadvantages of involving the use of a radioactive tracer and technical difficulties with external γ-probe counting. It also has the disadvantage of poor spatial resolution imaging, which limits its value for

[1] To whom correspondence and reprint requests should be addressed at Department of Surgery, School of Medicine, Keio University, 35 Shinanomachi, Shinjuku-ku, Tokyo, Japan, 160-8582. E-mail: m_ueda@sc.itc.keio.ac.jp.

0022-4804/$36.00

an accurate identification of the detailed anatomy of the draining lymphatic basin. Difficulty in identifying the location of lymph nodes presents an impediment to precise surgery.

The SLN concept also appears to be applicable to gastrointestinal cancers, and SLN detection may contribute to minimally invasive surgery, selective lymphadenectomy, and accurate staging by the lymphoscintigraphic method with intraoperative γ probe counting [4–8]. However, this method cannot be used for preoperative analysis of the accurate anatomic location of the SLN because of its limited spatial resolution [6, 7].

Lymphangiography by computed tomography (CT) has recently been reported to be feasible [9–12], but MRI has a number of potential advantages over lymphoscintigraphy and CT lymphangiography, including higher spatial resolution that enables depiction of lymphatic channels, higher temporal resolution, acquisition of three-dimensional images, and the absence of exposure to ionizing radiation.

Recent studies have shown the potential of magnetic resonance imaging (MRI) after interstitial administration of superparamagnetic iron oxide (SPIO) and ultrasmall superparamagnetic iron oxide (USPIO) in both animals [13–19] and humans [20–22]. However, according to the previous reports on MR lymphography, SPIO and USPIO were not retained in the sentinel lymph node (SLN) and flowed through it to the next nodes in line very soon after the injection. The ideal SLN imaging agent needs to have a particle size small enough to enter the lymphatic vessels, yet large enough to be retained in the SLN.

Newly developed thermoresponsive magnetic nanoparticles (Therma-Max; Magnabeat, Chiba, Japan) undergo a reversible transition between dispersion and aggregation as a function of temperature. The hypothesis that we tested in this study is that these magnetic nanoparticles are small enough to enter the lymphatic vessels, but then aggregate at body temperature and become large enough to be retained in the SLN, and will be useful for SLN mapping by MRI. In this study, we investigated the ability of MRI with thermoresponsive magnetic nanoparticles to detect SLN.

MATERIALS AND METHODS

Contrast Agents

The thermoresponsive property of Therma-Max derives from the N-isopropyl acrylamide coating of magnetic nanoparticles. Therma-Max undergoes a reversible transition between dispersion and aggregation as a function of temperature (Fig. 1). It has a low critical solution temperature of around 34°C and becomes insoluble at higher temperatures. The insoluble N-isopropyl acrylamide causes the magnetic nanoparticles to aggregate, and they are quickly separated from the solution in a magnetic field. The temperature at which they aggregate can be changed by adjusting dose of N-isopropyl acrylamide. The properties of Therma-Max have been described in detail by Kondo *et al.* [23].

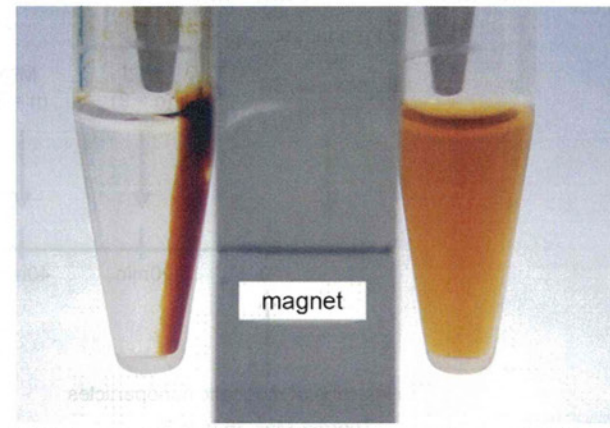

FIG. 1. The heated Therma-Max nanoparticles on the left aggregated and responded to the magnet (A). The cooled Therma-Max nanoparticles on the right did not aggregate and the nanoparticles solution did not respond to the magnet (B). Therma-Max showed a reversible transition between dispersion and aggregation as a function of temperature. (Color version of figure is available online.)

MR Imaging

All MRI examinations were performed with a 4.7-T MR unit (Varian INOVA, Varian Inc., Palo Alto, CA). The MRI protocol started with a T1-weighted gradient-echo localizer sequence composed of three section stacks oriented in the coronal and transverse planes. The MR imaging parameters were as follows: TE/TR 20/2000 ms, field of view (FOV) 10 × 5 cm, slice thickness 1 mm, and number of excitations 4.

Phantom Experiment

The phantom was constructed in a concentric manner from cylindrical plastic bottles containing the following substances from the core to the exterior: water, air. This phantom was scanned at various echo times (TEs) and a fixed repetition time (TR; 180 ms). The particles had a T1 relaxivity of 48.8 $mM^{-1}s^{-1}$ and a T2 relaxitivity of 726.4 $mM^{-1}s^{-1}$ (determined in aqueous solution, 37°C).

Image Interpretation and Data Analysis

The signal intensity of muscle tissue served as an internal standard for calculating the standardized signal intensity of a lymph node according to the following formula: SI = IL/IM, where SI = standardized signal intensity, IL = signal intensity of the lymph node, and IM = signal intensity of the muscle tissue. The reduced signal intensity (SI red) of a lymph node was calculated as follows: SI red (%) = (SI post − SI pre)/(SI pre × 100), where SI pre is the precontrast standardized signal intensity of the lymph node and SI post is the postcontrast standardized signal intensity of the lymph node. Differences between SI pre and SI post were tested for statistical significance by using Wilcoxon's test for paired samples. Differences between the SI of the SLN and that of a distant lymph node were tested by Fischer's exact test. A P value <0.05 was considered to indicate statistical significance.

Animals and Anesthesia

All animal studies were approved by the institutional review board for animal research. The animals used were 6-wk-old Donryu rats weighing 180–200 g. The body temperature of the rats was 38.5 ± 0.4°C. The

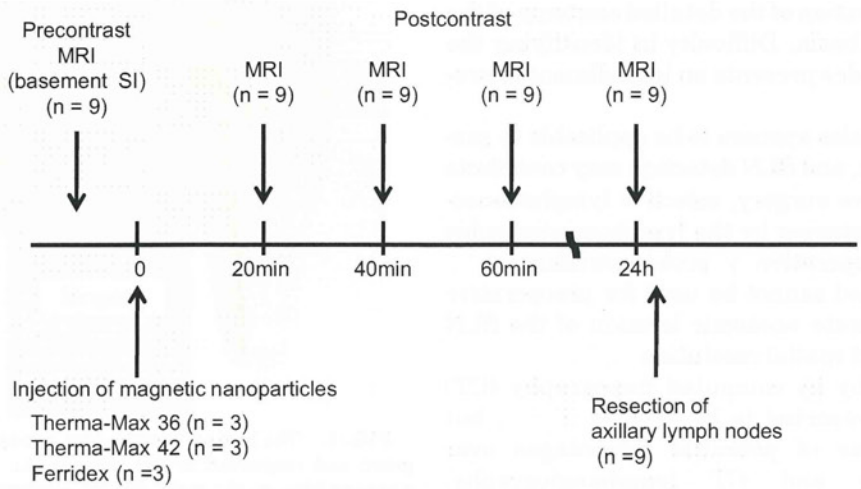

FIG. 2. The scheme of axillary SLN mapping with MRI. A precontrast MRI lymphogram was obtained, and postcontrast MRI lymphograms were obtained 20, 40, 60, min, and 24 h after injection of the magnetic nanoparticles.

injection of magnetic nanoparticles, resection of lymph nodes and injection sites, and histologic evaluation of lymph nodes in the mesentery were conducted with the animals sedated with an intraperitoneal injection of ketamine hydrochloride (50 mg per kilogram body weight ketavet; Parke-Davis, Berlin, Germany). MRI was performed under general anesthesia. All animals were killed by exsanguinations under deep anesthesia.

Axillary SLN Mapping with Magnetic Nanoparticles

Three types of magnetic nanoparticles were assessed; Therma-Max nanoparticles that aggregate at 36°C (Therma-Max 36), Therma-Max nanoparticles that aggregate at 42°C (Therma-Max 42), and magnetic nanoparticles not coated with a thermoresponsive polymer (Ferridex; Eiken Chemical Co., Tokyo, Japan). All of them were diluted with saline and contained 0.6 mg/mL of iron.

The diameter of all nanoparticles as measured by dynamic light scattering was approximately 100 nm, which is a favorable size for entering lymphatic vessels and reaching lymph nodes. A 1.0 mL syringe and a 26 gauge needle were used to subcutaneously inject 0.1 mL of the nanoparticle solution at five points on the right side of the thoracic wall of three rats each. A precontrast MRI lymphogram was obtained, and postcontrast MRI lymphograms were obtained 20, 40, 60 min, and 24 h after injection of the contrast material. Subcutaneous injection of isosulfan blue (lymphazurin; Covidien, Mansfield, MA) into the thoracic wall of the rats was performed to visualize the location of the axillary SLN, and they were resected and histologically examined with Prussian blue. The scheme of axillary SLN mapping with MRI was shown in Figure 2.

Intestinal SLN Mapping with Magnetic Nanoparticles

Injection of lymphazurin into the subserosa of cecum of rats was performed to visualize the location of the SLN and distant lymph nodes in the mesentery (Fig. 3). Three types of magnetic nanoparticles were assessed; Therma-Max 36, Therma-Max 42, and Therma-Max nanoparticles that aggregate at 55°C (Therma-Max 55). A 1.0 mL syringe and a 26 gauge needle were used to inject 0.04 mL of the nanoparticles solution at five points in the subserosal layer of the cecum of ten rats each. The SLN and the distant lymph nodes were resected at 5 min, 1, 4, 8, 12, and 24 h, and 2, 3, 5, and 7 d after the injection and examined histologically. All excised LNs and the injection sites were histologically evaluated after staining with Prussian blue. The scheme of intestinal SLN mapping with magnetic nanoparticles was shown in Figure 4.

RESULTS

Axillary SLN Mapping with Magnetic Nanoparticles

Isosulufan blue injection after MRI confirmed the location of the SLN. The location and the size of the SLNs at necropsy were consistent with the MRI findings. The postcontrast MRI findings following subcutaneous injection of Therma-Max 36 showed no marked changes in the SI of the axillary SLN. Histologic evaluation showed no influx of magnetic nanoparticles into the SLN. Postcontrast MRI following subcutaneous injection of Therma-Max 42 showed reduced SI of the axillary SLN (Fig. 5A and B). Histologic evaluation of the axillary SLN showed no magnetic nanoparticles before the injection and the presence of magnetic nanoparticles after the injection (Fig. 5C and D). Postcontrast MRI following subcutaneous injection of Ferridex showed reduced SI of the axillary SLN. Histologic

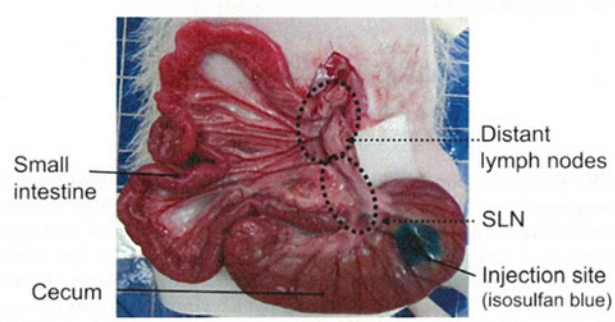

FIG. 3. Mesentery lymph nodes in rats. Injection of isosulfan blue into the subserosa of cecum visualized the location of SLNs and distant lymph nodes. (Color version of figure is available online.)

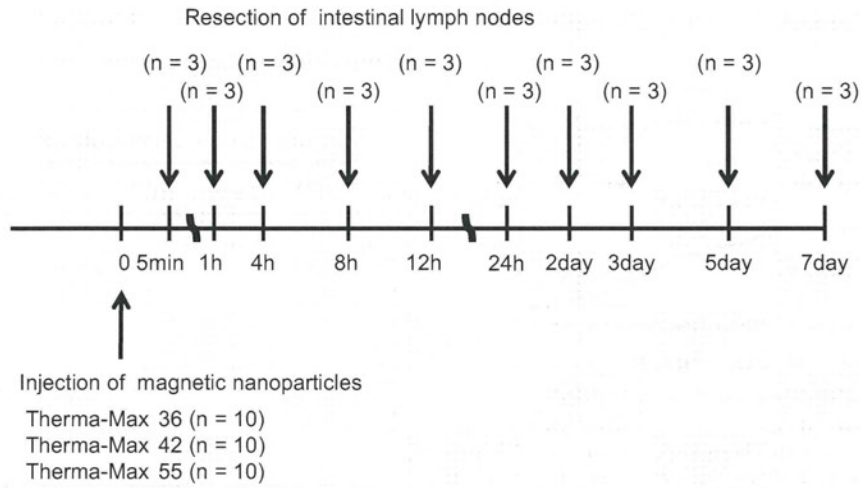

FIG. 4. The scheme of intestinal SLN mapping with magnetic nanoparticles. The SLN and the distant lymph nodes were resected at 5 min, 1, 4, 8, 12, and 24 h, and 2, 3, 5, and 7 d after the injection and examined histologically.

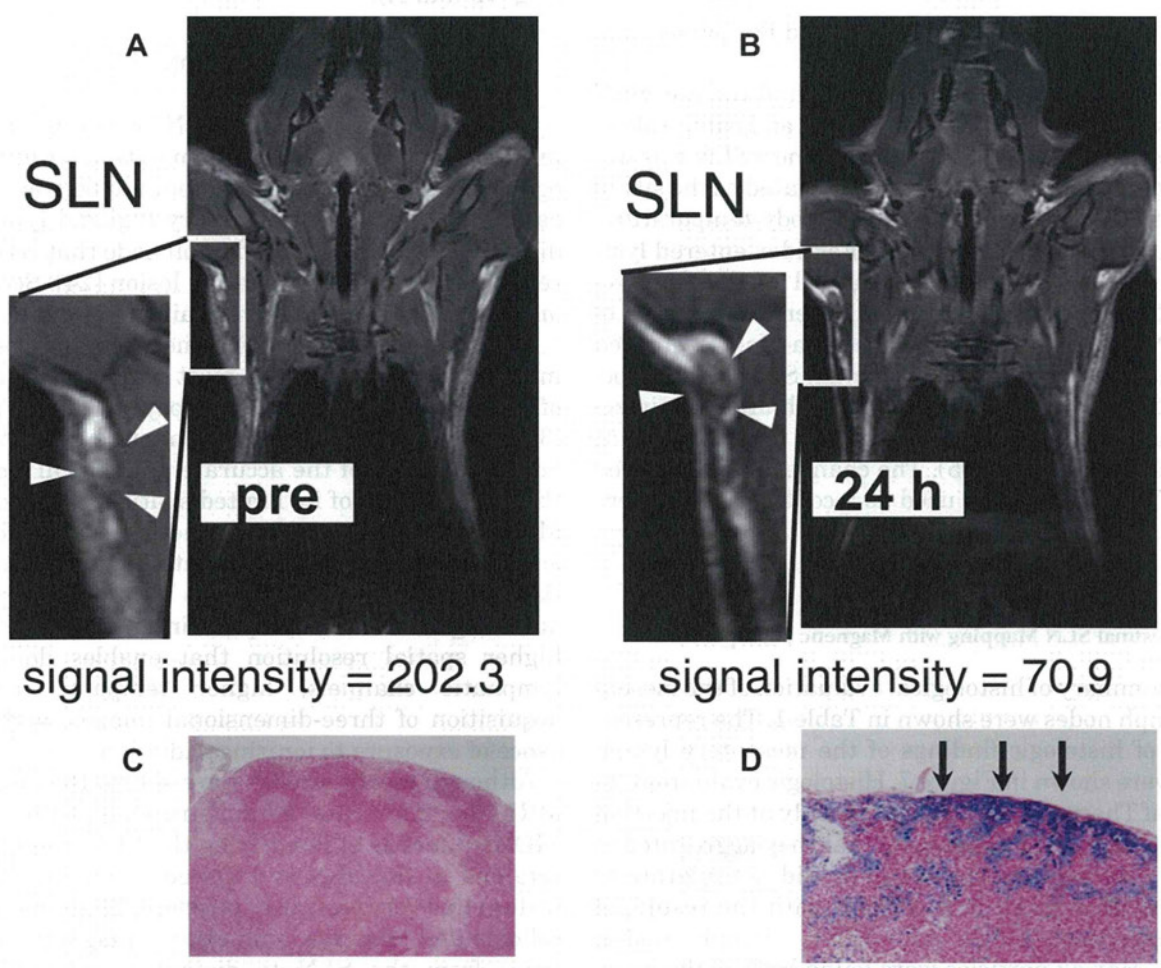

FIG. 5. Pre- and postcontrast MRI following subdermal injection of Therma-Max 42. (A) Precontrast MRI showed the axillary lymph node (arrowheads) with baseline signal intensity. (B) Postcontrast MRI (24 h after injection) showed reduced signal intensity of the axillary SLN (arrowheads). (C) Histologic evaluation of precontrast SLN. (D) Histologic evaluation of postcontrast SLN revealed influx of magnetic nanoparticles (arrows). (Color version of figure is available online.)

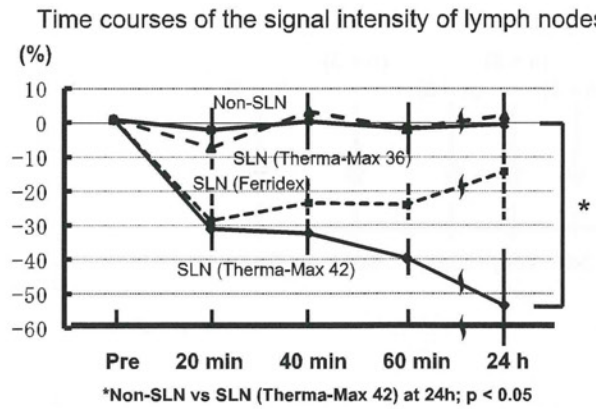

FIG. 6. The time courses of signal intensity (SI) of the SLN and distant LN. SI of either SLN with Therma-Max 36 or non-SLN was not changed. The minimum SI of the SLN with Ferridex occurred 20 min after the injection. The minimum SI of the SLN with Therma-Max 42 occurred 24 h after the injection. Twenty-four hours after the injection, the SI of SLN with Therma-Max 42 was significantly lower than that of non-SLN ($P < 0.05$). Therma-Max 42 made more remarkable changes of SI than Ferridex.

evaluation of the axillary SLN showed the presence of Ferridex nanoparticles.

The time courses of SI of the SLN and the non-SLN are shown in Figure 6. The non-SLN is an ipsilateral axillary lymph node. SI of the SLN and non-SLN was unchanged by Therma-Max 36. It aggregated at the site of injection as a result of exposure to body temperature, and did not migrate to the SLN. Ferridex entered lymphatic vessels, and the minimum SI of the SLN occurred 20 min after the injection, after which the SI of the SLN gradually increased. Therma-Max 42 entered lymphatic vessels, and the minimum SI of the SLN occurred 24 h after the injection. At 24 h after the injection, the SI of SLN was significantly lower than that of the non-SLN ($P < 0.05$). The changes in SI observed when Therma-Max was used as a contrast agent were greater than with Ferridex.

Intestinal SLN Mapping with Magnetic Nanoparticles

The summary of histological evaluation of the mesentery lymph nodes were shown in Table 1. The representatives of histologic findings of the mesentery lymph nodes were shown in Figure 7. Histologic evaluation revealed of Therma-Max 36 particles only at the injection site (Fig. 7A and B), suggesting that they aggregated in response to body temperature and did not migrate to the SLN. This result is consistent with the results of histological evaluation of axillary lymph nodes. Therma-Max 42 particles were found both at the injection site and in the SLN (Fig. 7C), but not in the distant lymph nodes (Fig. 7D). Therma-Max 55 and Ferridex particles were found at the injection site, in the SLN (Fig. 7E and G), and in the distant lymph nodes (Fig. 7F and H).

TABLE 1

Detection of Magnetic Nanoparticles in the Lymph Nodes

	Therma-Max 36		Therma-Max 42		Therma-Max 55		Ferridex	
Time	SLN	DLN	SLN	DLN	SLN	DLN	SLN	DLN
5 min	−	−	−	−	+	−	+	−
1 h	−	−	+	−	+	−	+	−
4 h	−	−	+	−	+	−	+	−
8 h	−	−	+	−	+	−	+	+
12 h	−	−	+	−	+	−	+	+
24 h	−	−	+	−	+	+	+	+
2 d	−	−	+	−	+	+	+	−
3 d	−	−	+	−	+	+	+	−
5 d	−	−	+	−	+	+	+	−
7 d	−	−	+	−	+	+	+	−

SLN = sentinel lymph node; DLN = distant lymph node.
+, detected; -, not detected.

DISCUSSION

Lymphatic mapping and SLN biopsy is one of the most interesting recent developments in surgical oncology. This approach allows patients to be treated in an early stage without unnecessary regional lymph node dissection. The SLN is the lymph node that receives direct drainage from the primary lesion [24]. Second-tier and third-tier nodes receive drainage in a later phase.

The lymphoscintigraphic method and blue dye method are currently the most widely used methods of identifying the SLN for biopsy in cancer patients [3]. However, these methods cannot be used for preoperative analysis of the accurate anatomical location of the SLN because of its limited spatial resolution [6, 7]. MR lymphography with magnetic nanoparticles will enable us to predict the accurate anatomic location of the SLN preoperatively. It has a number of potential advantages over lymphoscintigraphy, including higher spatial resolution that enables depiction of lymphatic channels, higher temporal resolution, acquisition of three-dimensional images, and the absence of exposure to ionizing radiation.

Although recent studies have shown the potential of MRI after interstitial administration of SPIO and USPIO as a means of identifying the SLN, they were not retained in the SLN and flowed through to the next node in line very soon after injection. The same as radiocolloids and blue dye, spill-over of magnetic nanoparticles from the SLN to distant lymph nodes may increase the labeling of non-SLNs. The interstitial MR lymphography with thermoresponsive magnetic nanoparticles adequately identified the axillary SLN.

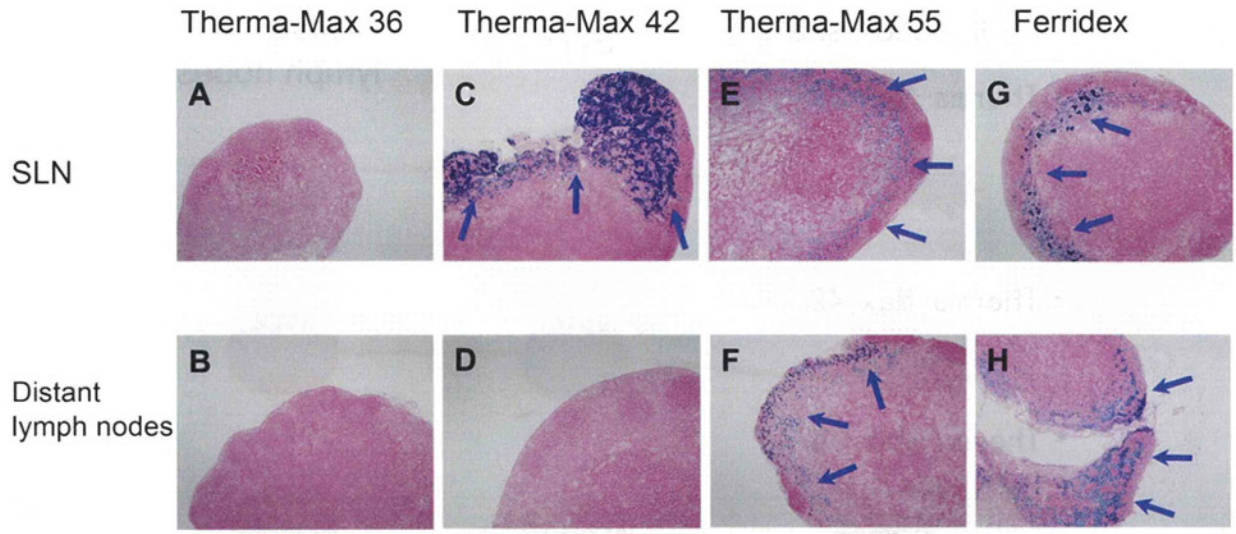

FIG. 7. The histologic evaluation of mesentery lymph nodes in rats. (A) SLN with Therma-Max 36 showed no magnetic nanoparticles. (B) Distant lymph nodes with Therma-Max 36 showed no magnetic nanoparticles. (C) SLN with Therma-Max 42 showed influx of magnetic nanoparticles (arrows). (D) Distant lymph nodes with Therma-Max 42 showed no magnetic nanoparticles. (E) SLN with Therma-Max 55 showed influx of magnetic nanoparticles (arrows). (F) Distant lymph nodes with Therma-Max 55 showed influx of magnetic nanoparticles (arrows). (G) SLN with Ferridex showed influx of magnetic nanoparticles (arrows). (H) Distant lymph nodes with Ferridex showed influx of magnetic nanoparticles (arrows). (Color version of figure is available online.)

Magnetic nanoparticles in the SLN can be detected with the newly developed superconducting quantum interference devices (SQUIDs) such as the SentiMag (Endomagnetics Ltd., London, U.K.). However, the SQUIDs require a large space and equipment. They are not useful when the SLN is located deep inside the body. MRI, on the other hand, has already been used clinically worldwide and is especially useful when the SLN is located deep inside the body. MRI is useful for preoperative SLN mapping with thermoresponsive magnetic nanoparticles and SQUIDs might be useful for intraoperative SLN mapping with thermoresponsive magnetic nanoparticles.

The intestinal SLN mapping in this study revealed that thermoresponsive magnetic nanoparticles could be specifically targeted to the SLN by adjusting the temperature at which they aggregate (Fig. 8). Therma-Max 42 entered lymphatic vessels and the minimum SI of the SLN occurred at 24 h after the injection, suggesting that Therma-Max 42 had been retained in the SLN. Ferridex entered the lymphatic vessels, and the minimum SI of the SLN occurred 20 min after the injection, and then gradually increased, suggesting that Ferridex may pass through the SLN rapidly. Ferridex and Therma-Max 55 sometimes reached the distant lymph nodes. Therma-Max 42 resulted in more marked changes in SI as a contrast agent than Ferridex did, suggesting that Therma-Max may be a more sensitive tracer for MR lymphography. The changes in SI with Therma-Max were slower than with Ferridex. These findings suggest that clinical use of Therma-Max might be feasible, for example, for endoscopic injection to detect gastrointestinal SLNs.

Differentiation of the SLN from distant lymph nodes and lymph nodes draining other anatomical sites is critical to SLN biopsy because examining the true SLN for extensive histologic evaluation increases the accuracy of staging. Although Therma-Max does not have specific lymphotropic properties, it is likely that it drains from the interstitial space into lymphatic pathways through thin-walled fenestrated lymphatic microvessels, similar to other extracellular, water-soluble, low-molecular solutes. The locations and the sizes of the SLNs resected from the animals at necropsy *post mortem* in our animals appeared to be consistent with the MR lymphography findings. Although these are preliminary results obtained in tumor-free animals, this method may have potential as a means of SLN mapping that will enable more precise and minimally invasive SLN biopsy.

Evaluation for toxicities of magnetic nanoparticles is mandatory. Unfortunately, no data about toxicities of magnetic nanoparticles in human being has been obtained. At least no side effects, including allergic reactions, were recognized in rats in this study. We plan to validate the SLN mapping with MRI using Therma-Max and to evaluate toxicities in larger animals.

In conclusion, MR lymphography with Therma-Max enables visualization of SLN. This method will reduce the labeling of non-SLNs seen in previous reports on interstitial MR lymphography. Although further study is required to evaluate its clinical efficacy in other animals and in humans, and to compare it with

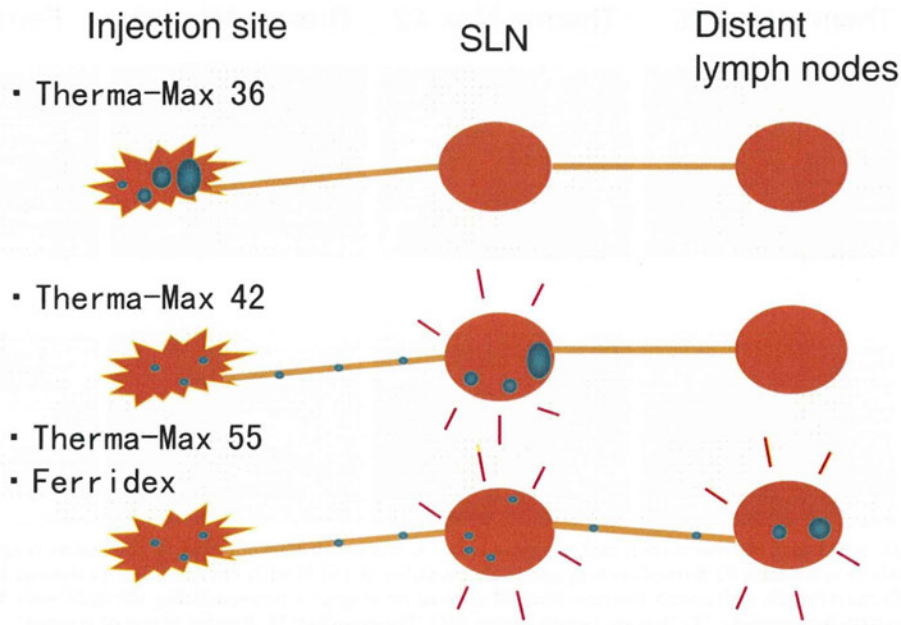

FIG. 8. Schema of each nanoparticle to identify the SLN. Therma-Max 36 aggregated at the site of injection according to body temperature and did not migrate to the SLN. Therma-Max 42 entered lymphatic vessels. It gradually aggregated according to body temperature and became large enough to be retained in the SLNs. Therma-Max 55 and Ferridex did not aggregate according to body temperature in rats. It also migrated to distant LNs. (Color version of figure is available online.)

scintigraphic and blue-dye methods, it may be an ideal method for achieving minimally invasive surgery in early stage cancers.

ACKNOWLEDGMENTS

The authors acknowledge support for this work by JSPS KAKENHI 20790938.

REFERENCES

1. Veronesi U, Galimberti V, Zurrida S, et al. Sentinel lymph node biopsy as an indicator for axillary dissection in early breast cancer. Eur J Cancer 2001;37:454.
2. Schrenk P, Shamiyeh A, Wayand W. Sentinel lymph-node biopsy compared to axillary lymph-node dissection for axillary staging in breast cancer patients. Eur J Surg Oncol 2001;27:378.
3. Krag D. Minimal invasive staging for breast cancer: Clinical experience with sentinel lymph node biopsy. Semin Oncol 2001; 28:229.
4. Kitagawa Y, Fujii H, Mukai M, et al. The role of the sentinel lymph node in gastrointestinal cancer. Surg Clin North Am 2000;80:1799.
5. Takeuchi H, Fujii H, Ando N, et al. Validation study of radio-guided sentinel lymph node navigation in esophageal cancer. Ann Surg 2009;249:757.
6. Kitagawa Y, Fujii H, Mukai M, et al. Radio-guided sentinel node detection for gastric cancer. Br J Surg 2002;89:604.
7. Kitagawa Y, Kitajima M. Gastrointestinal cancer and sentinel node navigation surgery. J Surg Oncol 2002;79:188.
8. Kitagawa Y, Ohgami M, Fujii H, et al. Laparoscopic detection of sentinel lymph nodes in gastrointestinal cancer: A novel and minimally invasive approach. Ann Surg Oncol 2001;8:86S.
9. Suga K, Yamamoto S, Tangoku A, et al. Breast sentinel lymph node navigation with three-dimensional interstitial multidetector-row computed tomographic lymphography. Invest Radiol 2005;40:336.
10. Suga K, Ogasawara N, Okada M, et al. Interstitial CT lymphography-guided localization of breast sentinel lymph node: Preliminary results. Surgery 2003;133:170.
11. Suga K, Yuan Y, Okada M, et al. Breast sentinel lymph node mapping at CT lymphography with iopamidol: Preliminary experience. Radiology 2004;230:543.
12. Hayashi H, Tangoku A, Suga K, et al. CT lymphography-navigated sentinel lymph node biopsy in patients with superficial esophageal cancer. Surgery 2006;139:224.
13. Hamm B, Taupitz M, Hussmann P, et al. MR lymphography with iron oxide particles: Dose-response studies and pulse sequence optimization in rabbits. AJR Am J Roentgenol 1992; 158:183.
14. Tanoura T, Bernas M, Darkazanli A, et al. MR lymphography with iron oxide compound AMI-227: Studies in ferrets with filariasis. AJR Am J Roentgenol 1992;159:875.
15. Weissleder R, Elizondo G, Josephson L, et al. Experimental lymph node metastases: Enhanced detection with MR lymphography. Radiology 1989;171:835.
16. Vassallo P, Matei C, Heston WD, et al. Characterization of reactive versus tumor-bearing lymph nodes with interstitial magnetic resonance lymphography in an animal model. Invest Radiol 1995;30:706.
17. Rogers JM, Jung CW, Lewis J, et al. Use of USPIO-induced magnetic susceptibility artifacts to identify sentinel lymph nodes and lymphatic drainage patterns. I. Dependence of artifact size with subcutaneous Combidex dose in rats. Magn Reson Imaging 1998;16:917.
18. Taupitz M, Wagner S, Hamm B, et al. Interstitial MR lymphography with iron oxide particles: Results in tumor-free and VX2 tumor-bearing rabbits. AJR Am J Roentgenol 1993;161:193.
19. Torchia MG, Nason R, Danzinger R, et al. Interstitial MR lymphangiography for the detection of sentinel lymph nodes. J Surg Oncol 2001;78:151. discussion 157.
20. McCauley TR, Rifkin MD, Ledet CA. Pelvic lymph node visualization with MR imaging using local administration of

ultra-small superparamagnetic iron oxide contrast. J Magn Reson Imaging 2002;15:492.
21. Imano H, Motoyama S, Saito R, et al. Superior mediastinal and neck lymphatic mapping in mid- and lower-thoracic esophageal cancer as defined by ferumoxides-enhanced magnetic resonance imaging. Jpn J Thorac Cardiovasc Surg 2004;52:445.
22. Ishiyama K, Motoyama S, Tomura N, et al. Visualization of lymphatic basin from the tumor using magnetic resonance lymphography with superparamagnetic iron oxide in patients with thoracic esophageal cancer. J Comput Assist Tomogr 2006; 30:270.
23. Kondo A, Kamura H, Higashitani K. Development and application of thermosensitive magnetic immunomicrospheres for antibody purification. Appl Microbiol Biotechnol 1994;41:99.
24. Nieweg OE, Tanis PJ, Kroon BB. The definition of a sentinel node. Ann Surg Oncol 2001;8:538.

Journal of Biotechnology 157 (2012) 124–129

Contents lists available at SciVerse ScienceDirect

Journal of Biotechnology

journal homepage: www.elsevier.com/locate/jbiotec

Protein-encapsulated bio-nanocapsules production with ER membrane localization sequences

Yuya Nishimura[a], Takuya Shishido[a], Jun Ishii[b], Tsutomu Tanaka[b], Chiaki Ogino[a], Akihiko Kondo[a,*]

[a] Department of Chemical Science and Engineering, Graduate School of Engineering, Kobe University, 1-1 Rokkodaicho, Nada-ku, Kobe 657-8501, Japan
[b] Organization of Advanced Science and Technology, Kobe University, Japan

ARTICLE INFO

Article history:
Received 11 July 2011
Received in revised form
14 September 2011
Accepted 16 September 2011
Available online 22 September 2011

Keyword:
Hepatitis B virus
Hepatitis B virus surface antigen
Drug delivery
Bio-nanocapsule
Encapsulation
Lipid modification

ABSTRACT

Bio-nanocapsules (BNCs) are hollow nanoparticles composed of the L protein of hepatitis B virus (HBV) surface antigen (HBsAg), which can specifically introduce genes and drugs into various kinds of target cells. Although the classic electroporation method has typically been used to introduce highly charged molecules such as DNA, it is rarely adopted for proteins due to its very low efficiency. In this study, a novel approach to the preparation of BNC was established whereby a target protein was pre-encapsulated during the course of nanoparticle formation. Briefly, because of the process of BNC formation in a budding manner on the endoplasmic reticulum (ER) membrane, the association of target proteins to the ER membrane with lipidation sequences (ER membrane localization sequences) could directly generate protein-encapsulating BNC in collaboration with co-expression of the L proteins. Since the membrane-localized proteins are automatically enveloped into BNCs during the budding event, this method can be protect the proteins and BNCs from damage caused by electroporation and obviate the need for laborious consideration to study the optimal conditions for protein encapsulation. This approach would be a useful method for encapsulating therapeutic candidate proteins into BNCs.

1. Introduction

Over the past couple of decades, drug delivery systems (DDS) have been intensively studied in order to improve the efficacy of chemotherapy and reduce its adverse effects. The delivery of bioactive molecules such as genes, chemical compounds and proteins to target cells is very significant for medical and biological applications (Nagai, 2005; Tabata, 2006). For this reason, it is necessary to establish an efficient carrier that ensures the internal stability of bioactive molecules, as well as their delivery into the targeted cells.

The bio-nanocapsule (BNC) is an attractive carrier for the delivery of bioactive molecules (Yamada et al., 2003). BNCs are hollow particles composed of the L protein of the hepatitis B virus (HBV), surface antigen (HBsAg), and the lipid bilayer derived from host cells (Kuroda et al., 1992). As carriers for drug delivery, these virus-like particles have many advantages, as follows: high specificity for human hepatocytes; high transfection efficiency, equivalent to the original HBV; reliable safety arising from the absence of the viral genome; high stability in the blood; and, a high capacity for encapsulation of genes and drugs (Yamada et al., 2003; Iwasaki et al., 2007; Jung et al., 2008).

To target cells other than hepatocytes, the specificity of BNC can be altered by genetic modifications. Varieties of specificity-altered BNCs have been produced by deleting the preS region having specificity for hepatocytes in the L protein, and inserting binding molecules targeting other cells (Kasuya et al., 2008, 2009). Antibodies and peptides have often been selected as such affinity molecules. To confer specificity for various kinds of cell surface receptors, antibody-mediated targeting with the ZZ domain (derived from protein A) or with biotin, which binds to the Fc region of immunoglobulin G (IgG) or streptavidin, has been developed as a practical and versatile technique (Iijima et al., 2011; Shishido et al., 2009a). Similarly, affibody molecules, which comprise a new class of affinity ligands derived from the Z domain and bind a range of different proteins, e.g. insulin, HER2 and EGFR, were used as a substitute for antibodies, while an arginine-rich peptide was displayed on BNC to permit the delivery into various types of cells (Nygren, 2008; Shishido et al., 2009b).

Abbreviations: DDS, drug delivery system; BNC, bio-nanocapsule; HBV, hepatitis B virus; HBsAg, hepatitis B virus surface antigen; ER, endoplasmic reticulum; IgG, immunoglobulin G; HER2, human EGFR-related 2; EGFR, epidermal growth factor receptor; MLS, membrane localization sequence; EGFP, enhanced green fluorescent protein; PCR, polymerase chain reaction; PEG, polyethylene glycol; PBS, phosphate-buffered saline; CsCl, discontinuous cesium chloride; EDTA, ethylene diamine tetraacetic acid; EIA, enzyme immunoassay; SDS-PAGE, sodium dodecyl sulphate-polyacrylamide gel electrophoresis electrotransferred onto a; PVDF, polyvinilidene fluoride; AP, alkaline phosphatase; BCIP, 5-bromo-4-chloro-3-indolyl phosphate; NBT, nitro blue tetrazolium; DLS, dynamic light scattering.

* Corresponding author. Tel.: +81 78 803 6196; fax: +81 78 803 6196.
E-mail address: akondo@kobe-u.ac.jp (A. Kondo).

0168-1656/$ – see front matter © 2011 Elsevier B.V. All rights reserved.
doi:10.1016/j.jbiotec.2011.09.015

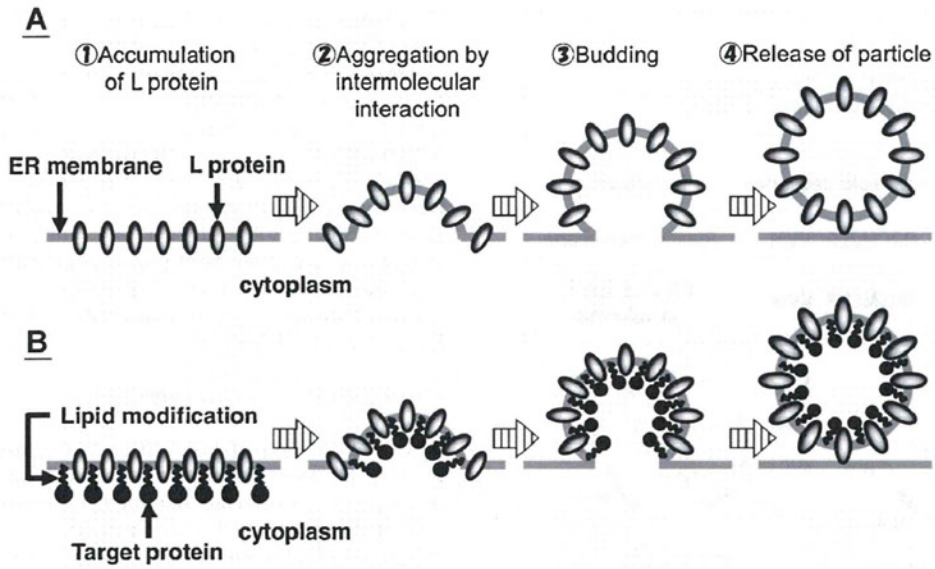

Fig. 1. Schematic illustration for the process of BNC formation in insect cells. (A) A common process of BNC formation. Translated L proteins are accumulated on the ER membrane and aggregated by intermolecular interaction. Hollow particles are released via budding events by self-assembly into the side of the ER lumen. (B) A strategy for direct production of protein-encapsulating BNC. Since target proteins are localized on the ER membrane by lipid modification, they are easily encapsulated inside BNC through the same process of common particle formation.

As described above, BNCs are useful carriers to deliver drugs specifically to different cell types. However, methods to encapsulate drugs into BNC have not been studied extensively. Therefore, the classic electroporation method is commonly used for this purpose (Yamada et al., 2003). Besides expensive equipment, this method requires consideration of the appropriate conditions that affect the encapsulation efficiency through various factors such as the intensity of electric voltage and pulse, temperature, concentration of particles and drugs, and composition of buffers (Yamada et al., 2003). Although electroporation has typically been used to introduce highly charged molecules such as DNA, it is rarely adopted for proteins due to its very low efficiency. Furthermore, many proteins, including pharmaceutical proteins, might suffer serious damage from high voltage, because they have a tendency to be denatured and agglutinated under severe conditions such as pH, heat and concentration (Chi et al., 2003). Thus, a simple and effective method for encapsulating proteins into BNC without using electroporation is needed.

In the present study, a novel approach to the preparation of BNC was established, in which a target protein is pre-encapsulated in the course of particle formation. We focused on the following mechanism for the formation of BNC (Fig. 1A): (1) L proteins localize and accumulate on the ER membrane; (2) aggregation of the L proteins is initiated by the accumulated L proteins on the ER; (3) intermolecular interactions trigger budding of the L particles; and, (4) hollow particles are formed within the ER lumen by a nucleocapsid-independent extrusion process and then exported from the cells via the vesicular transport pathway (Kuroda et al., 1992). BNC is thus produced when budding forms on the ER membrane. Therefore, the working assumption in the present study was that co-expression of the target proteins with the L proteins that associate with the outer leaflet of the ER membrane (cytoplasm side) by lipid modification could encapsulate the target proteins into the BNC, and would be accompanied by the formation of particles (Fig. 1B). As a means for this approach, lipidation sequences (membrane localization sequences; MLSs) derived from N-Ras, which cause prenylation in the CAAX motif (Choy et al., 1999), were added to the C-terminal of the target proteins. Since the ER membrane-localized target proteins were automatically embedded in the BNC during the formation process, this approach never required laborious consideration of the electroporation conditions after the preparation of hollow BNC particles, despite procedures identical to the previous process for the production and purification of BNC. We verified the feasibility of this strategy to encapsulate the target proteins into the BNC with lipidation motifs.

2. Materials and methods

2.1. Construction of plasmids for the expression of membrane-localized proteins in insect cells

MLS1 and MLS2 derived from N-Ras were selected as the lipidation sequences (Sato et al., 2006). The plasmids for expression of the enhanced green fluorescent protein (EGFP), attached with MLS1 or MLS2 in insect cells, were constructed as described below (Fig. 2A). The fragments encoding the EGFP-MLS1 or EGFP-MLS2 fusion gene were amplified by polymerase chain reaction (PCR) from pEGFP (Takara Bio, Shiga, Japan) with the following primers: EGFP-MLS1 (5′-GGGGGATCCATGGTGAGCAAGGGCGAGGA-3′ and 5′-GGGCCGC GGTTACATCACCACGCAGGGCAGGCCCATGCAGCCCTGCTTGTACAGC TCGTCCATGC-3′) and EGFP-MLS2 (5′-GGGGGATCCATGGTGAGCA AGGGCGAGGA-3′ and 5′-GGGCCGCGGTTACATCACCACGCAGGGCA GGCCCATGGAGCCCTGCTTGTACAGCTCGTCCATGC-3′). The amplified fragments were digested with *Bam*HI/*Sac*II and ligated into the pXIHAbla (Shishido et al., 2009c) (Fig. 2B). The resulting plasmids were designated as pXIHAbla-EGFP-MLS1 and pXIHAbla-EGFP-MLS2. The previously constructed plasmid pXIHAbla-EGFP (Shishido et al., 2009c) was used for the expression of cytosolic EGFP in a comparative expression manner. In contrast, plasmid pX-ML (Shishido et al., 2006) was used for the co-expression of BNC with these plasmids in insect cells (Fig. 2C).

2.2. Transfection of plasmids for the expression of EGFP-MLSs and/or BNC

A *Trichoplusia ni* BTI-TN-5B1-4 insect cell line (High Five) (Invitrogen, Carlsbad, CA, USA) was maintained in a serum-free medium (Express Five SFM) (Invitrogen) supplemented with 0.26 g/L

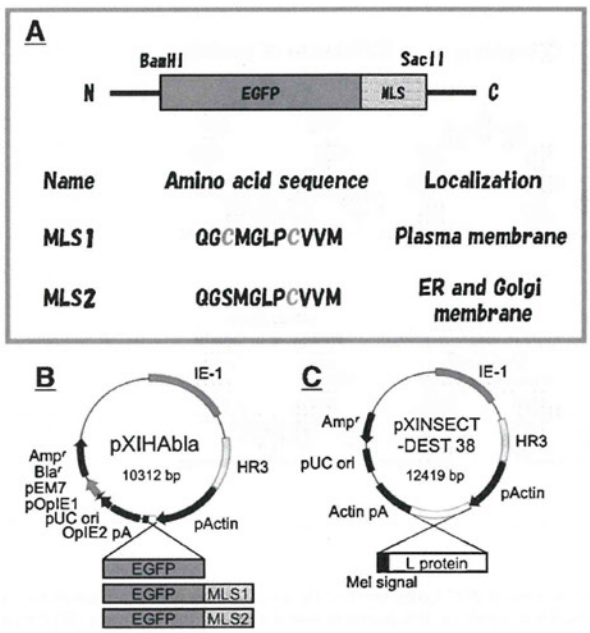

Fig. 2. Schematic representation of constructs to localize target proteins on the ER membrane of insect cells. ER membrane-localized proteins would be easily encapsulated into BNCs. (A) EGFP was used as a model for the target proteins. MLS1 and MLS2 derived from N-Ras were reported to localize on plasma or on the ER membrane in mammalian cells. Gray characters indicate the amino acid residues involved in lipid modifications. (B) Insect cell shuttle vector for expression of EGFP, EGFP-MLS1 and EGFP-MLS2. (C) Expression vector for secretion of BNC in insect cells.

L-glutamine and 10 mg/L gentamicin (Invitrogen) at 27 °C. High Five cells were seeded on a 35 mm dish at a density of 2×10^5 cells/ml for 24 h before transfection, and the cells were then used for transfection.

For observation by confocal laser scanning microscopy, the EGFP expression plasmid (pXIHAbla-EGFP, pXIHAbla-EGFP-MLS1 or pXIHAbla-EGFP-MLS2) was transfected into the High Five cells using FuGENE HD transfection reagent (Roche, Basel, Switzerland), following the manufacturer's procedure.

For purification of BNCs, pX-ML and EGFP expression plasmid (pXIHAbla-EGFP, pXIHAbla-EGFP-MLS1 or pXIHAbla-EGFP-MLS2) were co-transfected into High Five cells using FuGENE HD transfection reagent.

2.3. Confocal laser scanning microscopy observation of EGFP localization in insect cells

At 72 h after transfection, the cells were observed with a laser-scanning confocal microscope (Carl Zeiss, Oberkochen, Germany), following the manufacturer's procedure. Fluorescence images were acquired using the 488 nm line of an Ar laser for excitation and a 505 nm band pass filter for emission. The specimens were viewed using a 63-fold oil immersion objective.

2.4. Expression and purification of BNCs co-expressed with EGFP-MLSs

At 72 h after transfection, the culture supernatant (20 ml) of transfected insect cells was collected and mixed with polyethylene glycol (PEG) 6000 solution (33%, w/v). After 2 h incubation, the mixture was centrifuged at 10,000 × *g* for 30 min at 4 °C and the precipitate was dissolved in 2.8 ml of phosphate-buffered saline (PBS). The solution was layered onto a discontinuous cesium chloride (CsCl) gradient (11 ml, concentration: 10–40% (w/v) in buffer A [0.1 M sodium phosphate, 15 mM ethylene diamine tetraacetic acid (EDTA)]) and centrifuged at 24,000 rpm for 16 h at 15 °C in a himac CP70MXX centrifuge equipped with swing roter P40ST (Hitachi, Tokyo, Japan). The amount of BNC in each fraction was analyzed using an IMx enzyme immunoassay (EIA) kit (Abbott Laboratories, Abbott Park, IL, USA), following the manufacturer's procedure, and BNC was dialyzed against PBS. After dialysis, the BNC solution was layered onto a discontinuous sucrose gradient (11 ml, concentration: 10–50% (w/v) in buffer A) and centrifuged at 24,000 rpm for 10 h at 4 °C. The amount of BNC in each fraction was determined using the IMx EIA kit, and the expression of EGFP was confirmed by western blotting. Fractions containing BNC were dialyzed against PBS and stored at 4 °C.

2.5. SDS-PAGE and western blotting

The expression of EGFP in each fraction was confirmed by western blotting. The supernatant was fractionated by sodium dodecyl sulphate-polyacrylamide gel electrophoresis (SDS-PAGE) and electrotransferred onto a polyvinilidene fluoride (PVDF) membrane. Rabbit anti-EGFP antibodies (Medical Biological Laboratories, Nagoya, Japan) were used for immunoblotting, followed by anti-rabbit antibodies conjugated with alkaline phosphatase (AP) (Promega, Madison, WI, USA). The membrane was stained with 5-bromo-4-chloro-3-indolyl phosphate (BCIP) and nitro blue tetrazolium (NBT) (Promega).

2.6. Dynamic light scattering analysis of purified BNCs co-expressed with EGFP-MLSs

The size of the purified BNCs co-expressed with EGFP-MLSs was determined by dynamic light scattering (DLS) using a Zetasizer Nano particle size analyzer (Malvern Instruments Ltd., Worcestershire, UK), following the manufacturer's procedure.

3. Results and discussion

3.1. Strategy for direct production of protein-encapsulating BNC

The aim of the present study was to establish a novel approach that would enable the simple preparation of protein-encapsulating BNC. Because BNC is produced by a bioprocess, we hypothesized that BNC that inherently encapsulated the protein drug candidates could be prepared with genetic modifications. If protein-encapsulating BNC could be produced by the same process that is commonly used for preparing hollow BNC particles, this would permit the protection of BNC and proteins from damage caused by electroporation and obviate the need for laborious efforts to study the optimal conditions for protein encapsulation.

For these reasons, we focused on the formation mechanism of BNC, that is, budding on the ER membrane, as shown in Fig. 1A (Kuroda et al., 1992). We assumed that the co-expression of target proteins on the ER membrane might directly generate protein-encapsulating BNC by enveloping the membrane-localized proteins during the budding event (Fig. 1B). The strategy used to test the feasibility of this approach was to introduce MLSs into the C-terminus of the target proteins. Two types of peptide motifs, 11-amino-acid sequences derived from N-Ras including the CAAX motif, were selected as the MLSs for the lipidation. MLS1 (QGCMGLPCVVM) is lipidated through both prenylation at the cysteine residue on the CAAX motif and palmitoylation at the upstream cysteine residue (Choy et al., 1999) (Fig. 2A). However, MLS2 (QGSMGLPCVVM) is lipidated by only prenylation at the cysteine residue on the CAAX motif, since the Cys3 of MLS1 is replaced with a serine residue (Choy et al., 1999) (Fig. 2A). According to the literature, MLS1 was localized to the plasma membrane, and MLS2 was localized to the ER

membrane and golgi membrane apparatus in mammal cells (Sato et al., 2006). For the present study, an insect cell allowing secretory production of BNC (Shishido et al., 2006) was used as the host cell, and EGFP was used as the model target protein, which facilitated the evaluation of both localization and encapsulation of BNC.

3.2. Localization of target proteins with membrane localization sequences (MLSs) in insect cells

To confirm whether MLSs have ER membrane localization abilities in insect cells, plasmids were constructed expressing EGFP, EGFP-MLS1, and EGFP-MLS2 (Fig. 2B). These three types of plasmids were transfected into insect cells (High Five) without the plasmid producing BNC, and their localization was observed with a confocal laser-scanning microscope (Fig. 3).

Because of its lack of membrane localization ability, EGFP without MLS was observed in the cytoplasm of insect cells. EGFP-MLS1 was evenly localized on the plasma and ER membranes in insect cells, although MLS1 reportedly locates on the plasma membrane in mammal cells. In contrast, EGFP-MLS2 was strongly but partially localized to the ER membrane. Thus, in the present study, both MLS1 and MLS2 functioned as membrane localization sequences in insect cells and had the capacity to localize EGFP on ER membranes, even though they varied in their ER localization ability. This result indicates that both MLS1 and MLS2 are capable of localizing target proteins on an ER membrane as therapeutic candidates in a similar fashion.

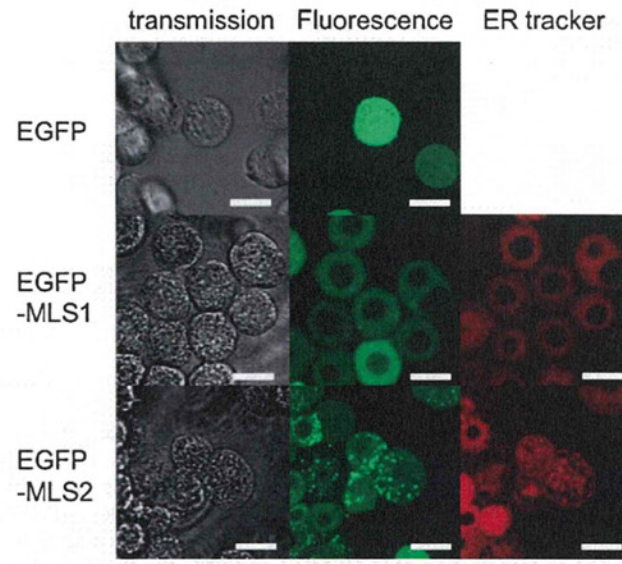

Fig. 3. Fluorescence images for observation of the localization of EGFP in insect cells with confocal microscopy. ER-tracker (Invitrogen) was used as the localization marker. The upper images are the cells transfected with EGFP expression plasmid. The middle images are the cells transfected with EGFP-MLS1 expression plasmid. The lower images are the cells transfected with EGFP-MLS2 expression plasmid. Scale bars; 20 μm.

3.3. Production and purification of EGFP-encapsulating BNC

To investigate the validity of our approach, the three types of plasmids (for expression of EGFP, EGFP-MLS1 and EGFP-MLS2) were co-transfected, with the plasmid producing BNC, into insect cells (High Five). After 72 h of cultivation, the supernatants were harvested and the BNCs were purified by gradient ultracentrifugation, as described in materials and methods. The resultant fractions were analyzed by EIA to measure the amount of BNC and by western blotting to evaluate whether the BNCs encapsulated EGFP (Fig. 4). After dialysis, about 25 μg of purified EGFP-MLS1/BNC

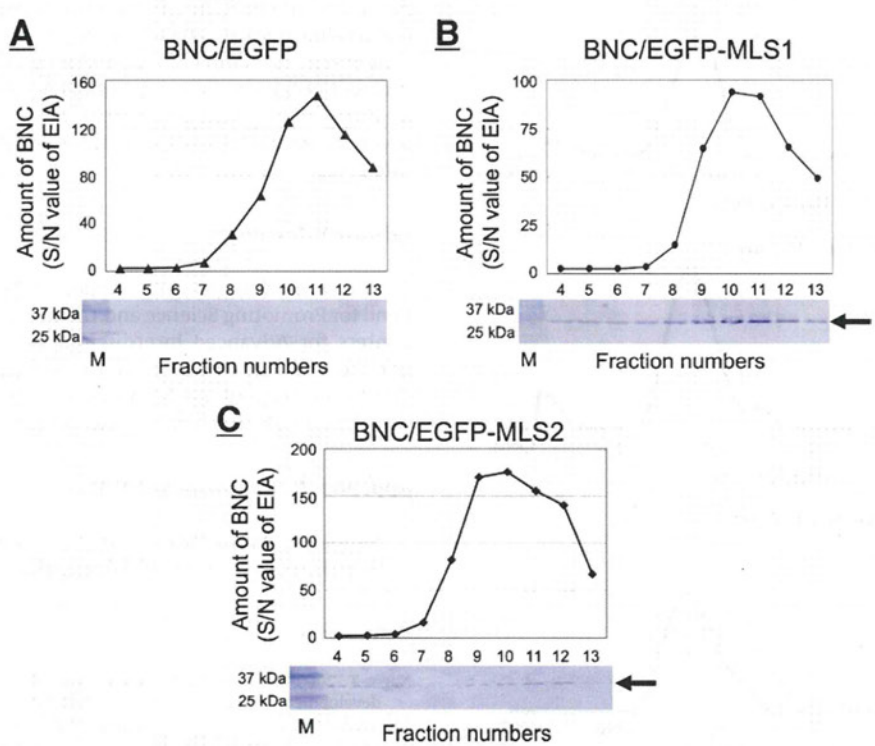

Fig. 4. Examination for encapsulation of EGFP into the purified BNCs. After sucrose gradient centrifugation, the amount of BNC including each fraction was measured with an IMx EIA kit (S/N value of EIA). The same fractions were tested for the presence of EGFP by western blotting with anti-EGFP antibody. Co-expression of (A) BNC and EGFP, (B) BNC and EGFP-MLS1, and (C) BNC and EGFP-MLS2.

Table 1
Purification summary of EGFP-MLS1/BNC and EGFP-MLS2/BNC.

Sample name	Step	Volume (ml)	Concentration (μg/ml)	Mass (μg)
EGFP-MLS1/BNC	Culture medium supernatant	20.0	2764.8	55,296.6
	Pellet after PEG settling method	2.8	1220.0	3416.0
	After CsCl ultracentrifugal method	3.0	54.9	164.6
	After Sucrose ultracentrifugal method	6.0	3.2	19.4
	After concentration	0.5	51.6	25.8
EGFP-MLS2/BNC	Culture medium supernatant	20.0	2683.6	53,672.3
	Pellet after PEG settling method	2.8	726.2	2033.3
	After CsCl ultracentrifugal method	3.0	58.1	174.3
	After Sucrose ultracentrifugal method	6.0	6.5	38.7
	After concentration	0.7	35.5	24.9

and EGFP-MLS2/BNC were obtained from 20 ml of culture medium supernatant (Table 1).

First, in the case of co-transfection of EGFP and BNC, although the main peaks of BNCs appeared in 10–12 fractions, the bands of EGFP were not detected in the same fractions (Fig. 4A). This result indicates that EGFP was not encapsulated in BNC, although BNC was produced uneventfully in the insect cells. Second, in the case of co-transfection of EGFP-MLS1 and BNC, the thick bands of EGFP were detected in 9–12 fractions, which displayed the main peaks of BNC (Fig. 4B). This suggests that EGFP-encapsulating BNC was successfully produced by introduction of the MLS1 motif. In the third case, co-transfection of EGFP-MLS2 and BNC displayed a result similar to the case of EGFP-MLS1 and BNC (Fig. 4C), suggesting that the introduction of MLS2 also allowed the production of EGFP-encapsulating BNC. The smaller amounts of EGFP in the BNC with MLS2 might be attributed to partial localization on the ER. However, since the EGFP-encapsulating BNC with MLS2 produced almost twice the amount of particles as that with MLS1, this suggests that MLS2 might be a better expression system for protein-encapsulating BNC (Fig. 4B and 4C). These differences might be due to the presence or absence of the palmitoylation site between MLS1 and MLS2.

Finally, the diameters of the BNC particles were evaluated using the DLS method (Fig. 5). The diameters of the three types of particles were almost equivalent, at 150 nm, indicating that the diameter of EGFP-encapsulating BNCs was similar to that of hollow BNC particles produced in insect cells (Kurata et al., 2008). In addition, it was also confirmed that the EGFP-encapsulating BNCs kept the targeting abilities to human hepatocytes (Supplementary Fig. 1).

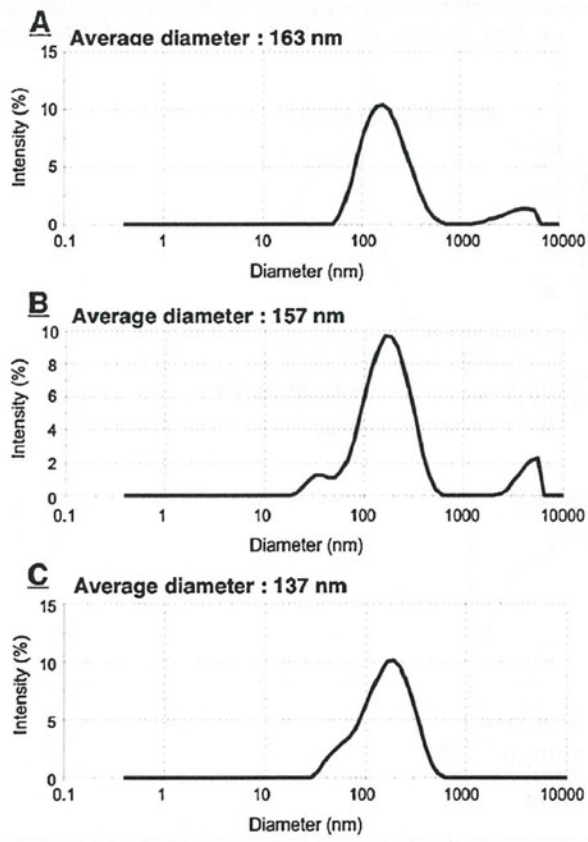

Fig. 5. DLS analyses of purified BNCs. Co-expression of (A) BNC and EGFP, (B) BNC and EGFP-MLS1, and (C) BNC and EGFP-MLS2.

4. Conclusions

The feasibility of this approach to the direct production of protein-encapsulating BNC by localizing the target proteins on the ER membrane was successfully demonstrated. In this study, MLS1 and MLS2 of N-Ras were used to localize the target proteins on the ER membrane either by prenylation or by palmitoylation. While MLS1 and MLS2 could incorporate our approach, other ER membrane localization sequences with different modification mechanisms might also be utilized to produce protein-encapsulating BNCs. In addition, whereas therapeutic candidate proteins might be encapsulated in BNC in the same manner as EGFP, this should be demonstrated in the near future. This approach would be a useful tool for encapsulating target proteins into BNCs.

Acknowledgements

This work was partially supported by a Special Coordination Fund for Promoting Science and Technology, Creation of Innovative Centers for Advanced Interdisciplinary Research Areas (Innovative Bioproduction Kobe) from the Ministry of Education, Culture, Sports and Technology (MEXT), and Science Research Grants from the Ministry of Health, Labor and Welfare, Japan.

Appendix A. Supplementary data

Supplementary data associated with this article can be found, in the online version, at doi:10.1016/j.jbiotec.2011.09.015.

References

Nagai, T., 2005. Drug discovery and innovative drug delivery research in new drug development. Pharm. Tech. Jpn. 21, 1949–1951.
Tabata, T., 2006. Drug delivery system: basic technology for biomedical research, medical treatment and health care. Biotechnol. J. 6, 553–555.
Yamada, T., Iwasaki, Y., Tada, H., Iwabuki, H., Chuah, M.K., VandenDriessche, T., Fukuda, H., Kondo, A., Ueda, M., Seno, M., Tanizawa, K., Kuroda, S., 2003. Nanoparticles for the delivery of genes and drugs to human hepatocytes. Nat. Biotechnol. 21, 885–890.

Kuroda, S., Otaka, S., Miyazaki, T., Nakao, M., Fujisawa, Y., 1992. Hepatitis B virus envelope L protein particles. Synthesis and assembly in *Saccharomyces cerevisiae*, purification and characterization. J. Biol. Chem. 267, 1953–1961.

Iwasaki, Y., Ueda, M., Yamada, T., Kondo, A., Seno, M., Tanizawa, K., Kuroda, S., Sakamoto, M., Kitajima, M., 2007. Gene therapy of liver tumors with human liver-specific nanoparticles. Cancer Gene Ther. 14, 74–81.

Jung, J., Matsuzaki, T., Tatematsu, K., Okajima, T., Tanizawa, K., Kuroda, S., 2008. Bio-nanocapsule conjugated with liposomes for in vivo pinpoint delivery of various materials. J. Control. Release 126, 255–264.

Kasuya, T., Jung, J., Kadoya, H., Matsuzaki, T., Tatematsu, K., Okajima, T., Miyoshi, E., Tanizawa, K., Kuroda, S., 2008. In vivo delivery of bionanocapsules displaying phaseolus vulgaris agglutinin-L_4 isolectin to malignant tumors overexpressing N-acetylglucosaminyltransferase V. Hum. Gene Ther., 887–895.

Kasuya, T., Jung, J., Kinoshita, R., Goh, Y., Matsuzaki, T., Iijima, M., Yoshimoto, N., Tanizawa, K., Kuroda, S., 2009. Bio-nanocapsule–liposome conjugates for in vivo pinpoint drug and gene delivery. Methods Enzymol. 464, 147–166.

Iijima, M., Kadoya, H., Hatahira, S., Hiramatsu, S., Jung, G., Martin, A., Quinn, J., Jung, J., Jeong, S.Y., Choi, E.K., Arakawa, T., Hinako, F., Kusunoki, M., Yoshimoto, N., Niimi, T., Tanizawa, K., Kuroda, S., 2011. Nanocapsules incorporating IgG Fc-binding domain derived from *Staphylococcus aureus* protein A for displaying IgGs on immunosensor chips. Biomaterials 32, 1455–1464.

Shishido, T., Azumi, Y., Nakanishi, T., Umetsu, M., Tanaka, T., Ogino, C., Fukuda, H., Kondo, A., 2009a. Biotinylated bionanocapsules for displaying diverse ligands toward cell-specific delivery. J. Biochem. 146, 867–874.

Nygren, P.A., 2008. Alternative binding proteins: affibody binding proteins developed from a small three-helix bundle scaffold. FEBS J. 275, 2668–2676.

Shishido, T., Yonezawa, D., Iwata, K., Tanaka, T., Ogino, C., Fukuda, H., Kondo, A., 2009b. Construction of arginine-rich peptide displaying bionanocapsules. Bioorg. Med. Chem. Lett. 19, 1473–1476.

Chi, E.Y., Krishnan, S., Randolph, T.W., Carpenter, J.F., 2003. Physical stability of proteins in aqueous solution: mechanism and driving forces in nonnative protein aggregation. Pharm. Res. 20, 1325–1336.

Choy, E., Chiu, V.K., Silletti, J., Feoktistov, M., Morimoto, T., Michaelson, D., Ivanov, I.E., Philips, M.R., 1999. Endomembrane trafficking of ras: the CAAX motif targets proteins to the ER and Golgi. Cell 98, 69–80.

Sato, M., Ueda, Y., Umezawa, Y., 2006. Imaging diacylglycerol dynamics at organelle membranes. Nat. Methods 3, 797–799.

Shishido, T., Kurata, N., Yoon, M.E., Tanaka, T., Yamaji, H., Fukuda, H., Kondo, A., 2009c. A high-level expression vector containing selectable marker for continuous production of recombinant protein in insect cells. Biotechnol. Lett. 31, 623–627.

Shishido, T., Muraoka, M., Ueda, M., Seno, M., Tanizawa, K., Kuroda, S., Fukuda, H., Kondo, A., 2006. Secretory production system of bionanocapsules using a stably transfected insect cell line. Appl. Microbiol. Biotechnol. 73, 505–511.

Kurata, N., Shishido, T., Muraoka, M., Tanaka, T., Ogino, C., Fukuda, H., Kondo, A., 2008. Specific protein delivery to target cells by antibody-displaying bionanocapsules. J. Biochem. 144, 701–707.

Ultrasonics Sonochemistry 19 (2012) 607–614

Contents lists available at SciVerse ScienceDirect

Ultrasonics Sonochemistry

journal homepage: www.elsevier.com/locate/ultsonch

Targeted sonodynamic therapy using protein-modified TiO_2 nanoparticles

Kazuaki Ninomiya [a], Chiaki Ogino [b], Shuhei Oshima [c], Shiro Sonoke [c], Shun-ichi Kuroda [d], Nobuaki Shimizu [a,*]

[a] Institute of Nature and Environmental Technology, Kanazawa University, Kanazawa 920-1192, Japan
[b] Department of Chemical Science and Engineering, Graduate School of Engineering, Kobe University, Kobe 657-8501, Japan
[c] Division of Material Engineering, Graduate School of Natural Science and Technology, Kanazawa University, Kanazawa 920-1192, Japan
[d] Department of Bioengineering Sciences, Graduate School of Bioagricultural Sciences, Nagoya University, Nagoya 464-8601, Japan

ARTICLE INFO

Article history:
Received 13 August 2011
Received in revised form 13 September 2011
Accepted 22 September 2011
Available online 4 October 2011

Keywords:
Ultrasound
Titanium dioxide
Nanoparticles
Pre-S1/S2
Sonodynamic therapy

ABSTRACT

Our previous study suggested new sonodynamic therapy for cancer cells based on the delivery of titanium dioxide (TiO_2) nanoparticles (NPs) modified with a protein specifically recognizing target cells and subsequent generation of hydroxyl radicals from TiO_2 NPs activated by external ultrasound irradiation (called TiO_2/US treatment). The present study first examined the uptake behavior of TiO_2 NPs modified with pre-S1/S2 (model protein-recognizing hepatocytes) by HepG2 cells for 24 h. It took 6 h for sufficient uptake of the TiO_2 NPs by the cells. Next, the effect of the TiO_2/US treatment on HepG2 cell growth was examined for 96 h after the 1 MHz ultrasound was irradiated (0.1 W/cm^2, 30 s) to the cells which incorporated the TiO_2 NPs. Apoptosis was observed at 6 h after the TiO_2/US treatment. Although no apparent cell-injury was observed until 24 h after the treatment, the viable cell concentration had deteriorated to 46% of the control at 96 h. Finally, the TiO_2/US treatment was applied to a mouse xenograft model. The pre-S1/S2-immobilized TiO_2 (0.1 mg) was directly injected into tumors, followed by 1 MHz ultrasound irradiation at 1.0 W/cm^2 for 60 s. As a result of the treatment repeated five times within 13 days, tumor growth could be hampered up to 28 days compared with the control conditions.

1. Introduction

Ultrasound has been widely utilized for medical diagnosis due to its ability to penetrate tissue with less attenuation of energy. Ultrasound is also applied to therapeutic use, typically for cancer therapy [1]. There are two uses for ultrasound in cancer therapy. One is for hyperthermic cancer therapy based on the thermal effect of high-intensity focused ultrasound [2]. The other is sonodynamic cancer therapy based on non-thermal and sonochemical effects from the combination of low-intensity ultrasound and sonosensitizer (e.g. anti-cancer drugs or certain chemicals) which exhibit the preferential uptake and/or accumulation in tumor tissues and subsequent activation by ultrasound irradiation [3–5]. In 1989, Umemura et al. [6] suggested sonodynamic therapy (SDT) for cancer cells using hematoporphyrin, formally known as a photosensitizer for photodynamic therapy (PDT) [7], since the clinical application of PDT is very limited to cancer at the surface region due to the inability of photo energy to penetrate deep tissues.

Titanium dioxide (TiO_2) has been generally known as photocatalyst, generating reactive oxygen species (ROS) under ultraviolet irradiation [8,9]. The ROS produced by the photocatalytic effect of TiO_2 particles has been applied to killing cancer cells [10–12] as well as the degradation of harmful chemicals and inactivation of microorganisms. From the viewpoint of practical application, some groups demonstrated that nanoparticles (NPs) of TiO_2 could be used as a photocatalyst for injuring cancer cells [13–16]. Moreover, it was reported that the surface of TiO_2 NPs was modified with antibody recognizing cancer cells in order to localize the ROS effect toward the targeted cells, and that the antibody-immobilized TiO_2 NPs could be used for the photocatalytic injury of cancer cells [17–19]. However, the problem of the superficially-limited therapeutic effect would remain as long as these kinds of TiO_2 photocatalysts are activated by photo-energy, like the photosensitizer in the PDT.

Recently, our group discovered that TiO_2 could act as a sonocatalyst; namely, the presence of TiO_2 particles could enhance the hydroxyl (OH) radical generation by ultrasound irradiation even in the dark without ultraviolet irradiation [20]. The sonocatalytic effect of TiO_2 (nano)particles has been applied to degradation of certain kinds of chemicals [21,22], and inactivation of microorganisms [23–26]. With regard to the application of the sonocatalytic effect of TiO_2 NPs on cancer cell injury, our previous study first demonstrated that TiO_2 NPs modified with a targeting protein could be incorporated in cancer cells, and activated sonocatalytically to generate OH radicals, resulting in damage to the cell membrane [27]. Recently, some groups also reported *in vitro* and *in vivo* SDT using

* Corresponding author. Tel.: +81 76 234 4807; fax: +81 76 234 4829.
E-mail address: nshimizu@t.kanazawa-u.ac.jp (N. Shimizu).

1350-4177/$ - see front matter © 2011 Elsevier B.V. All rights reserved.
doi:10.1016/j.ultsonch.2011.09.009